Physics-Inspired Deep Learning Anti-Aliasing Framework in Efficient Channel State Feedback

Yu-Chien Lin, Yan Xin, Ta-Sung Lee, Charlie (Jianzhong) Zhang, and Zhi Ding

***Abstract*—Acquiring downlink channel state information (CSI) at the base station is vital for optimizing performance in massive Multiple input multiple output (MIMO) Frequency-Division Duplexing (FDD) systems. While deep learning architectures have been successful in facilitating UE-side CSI feedback and gNB-side recovery, the undersampling issue prior to CSI feedback is often overlooked. This issue, which arises from low density pilot placement in current standards, results in significant aliasing effects in outdoor channels and consequently limits CSI recovery performance. The main objective of this work is to solve this issue by introducing a new CSI upsampling framework at the gNB as a post-processing solution to address the gaps caused by undersampling. Leveraging the physical principles of discrete Fourier transform shifting theorem and multipath reciprocity, our framework effectively uses uplink CSI to mitigate aliasing effects. We further develop a learning-based method that integrates the proposed algorithm with the Iterative Shrinkage-Thresholding Algorithm Net (ISTA-Net) architecture, enhancing our approach for non-uniform sampling recovery. Our numerical results show that both our rule-based and deep learning upsampling methods significantly outperform traditional interpolation techniques or multiple state-of-the-art approaches by 8-13 dB and 2-10 dB, respectively, in terms of normalized mean square error.**

***Index Terms*—Deep unfolding, CSI upsampling, massive MIMO, CSI recovery.**

I. Introduction

Massive multiple-input multiple-output (MIMO) technologies form a cornerstone of modern wireless communications, significantly enhancing both spectral and energy efficiency (SE and EE) at the base station, or gNodeB (gNB) [1], [2]. In frequency-division duplexing (FDD) systems, effective MIMO transmitters hinge on accurate downlink (DL) channel state information (CSI) acquisition at the gNB. Reliable DL CSI acquisition is crucial in massive MIMO to ensure optimal precoding and improved SE. However, acquiring DL CSI at FDD transmitters faces notable challenges due to feedback constraints.

Y.-C Lin and Z. Ding are with the Department of Electrical and Computer Engineering, University of California, Davis, CA, USA (e-mail: ycmlin, zding@ucdavis.edu).

Y. Xin and C. Zhang are with Samsung Research America, USA (e-mail: yan.xin, jianzhong.z@samsung.com).

T.-S Lee is with the Institute of Communications Engineering, National Yang Ming Chiao Tung University, Taiwan (e-mail: tslee@nycu.edu.tw).

This material is based upon work supported by the National Science Foundation under Grants 2009001 (Lin, Ding), by the Samsung GRO Program, and by the National Science & Technology Council of Taiwan grants NSTC 113-2218-E-A49-026, NSTC 113-2221-E-A49-118, NSTC 113-2622-E-A49-003 (Lee).

Unlike time-division duplex (TDD) systems, FDD systems generally cannot rely on channel reciprocity between the uplink (UL) and downlink (DL), necessitating CSI acquisition through feedback from user equipment (UE). This dependency on UE feedback introduces substantial overhead, as the feedback must convey a large volume of MIMO CSI coefficients, which is costly in terms of UL bandwidth and power consumption. To alleviate these burdens, efficient compressive feedback mechanisms are essential. Cellular CSI typically has a limited delay spread, which can be exploited for efficient CSI compression and recovery. One promising approach is to apply a deep autoencoder framework, as demonstrated in [3], which includes an encoder at the UE and a decoder at the serving gNB. Other related works have shown superior CSI recovery or lightweight design using various autoencoder models, including [4]–[7].

In addition to autoencoders, recent studies have leveraged underlying channel correlations to enhance DL CSI recovery at base stations (BSs), incorporating information from previous CSI [4], [8], CSI of nearby UEs [9], and UL CSI [10]–[12]. These methods leverage the inherent spatial and temporal correlation [4], [8] in wireless channels to improve estimation accuracy of CSI and reduce feedback payload. Furthermore, some works on deep learning-based CSI compressive feedback architectures have focused on reducing model complexity and storage requirements to enable practical and low-cost deployment [5], [7]. Despite these advances, achieving reliable DL CSI recovery with minimal feedback overhead remains a major challenge in massive MIMO FDD systems, motivating continued efforts to investigate efficient compression and recovery solutions.

An underlying assumption of many compressive feedback models is that the system employs dense pilot placement, enabling accurate full-CSI recovery at the UE from high-quality feedback. However, since the 5G standard's CSI reference signals (CSI-RS) are primarily designed for subband-level feedback, the CSI-RS placement is one element per one or two resource blocks (RBs), incapable of capturing the full granularity of the CSI structure at the subcarrier level [13], [14]. Recovering DL CSI at the subcarrier level requires an impractically high density CSI-RS placement to capture high-frequency variations caused by large-delay multipath components, which are particularly prominent in outdoor scenarios. Without sufficient CSI-RS density, aliasing can occur during the interpolation process, distorting the recovered CSI. This aliasing problem is a significant obstacle to effective DL CSI recovery, as illustrated below.

A. Aliasing Issue in Interpolation

From a signal processing standpoint, undersampling leads to an irreversible loss of high-frequency variations, resulting in the *aliasing effect in sub-Nyquist signal recovery*. Similarly by reversing time and frequency, when the CSI frequency sampling rate is less than twice the largest multipath delays of a CSI, delay domain aliasing occurs. In this case, multipaths with delays exceeding the measurable delay become ambiguous for the receiver (UE). The UE cannot recover these multipath components correctly, even with upsampling.

To relate this to practical values, consider various subcarrier spacings: with a 30 kHz spacing and CSI-RS placement every 1 RB (360 kHz frequency separation), the largest measurable delay is $1.39\,\mu$s. As subcarrier spacing increases to 60 kHz or 120 kHz—often used for mmWave or FR2 bands—the measurable delays reduce substantially. For a 60 kHz subcarrier spacing, the largest measurable delay is $0.694\,\mu$s at 1 RB density, reducing to $0.347\,\mu$s at 120 kHz spacing. At 120 kHz spacing with every 2 RBs for CSI-RS placement, the measurable delay drops to $0.174\,\mu$s.

Studies show that in sub-6 GHz bands, delay spreads can exceed $1\,\mu$s [15], [16]. Moreover, in about 20% of NLoS Urban Macro channel realizations, delay spreads surpass $1\,\mu$s [17]. Such delay spreads exceed the measurable limits, particularly in mmWave bands, where dense multipath reflections are common [18]. This results in unavoidable aliasing under such conditions, emphasizing the need for advanced upsampling techniques to reconstruct subcarrier-level CSI from RB-level CSI-RS in 5G NR environments

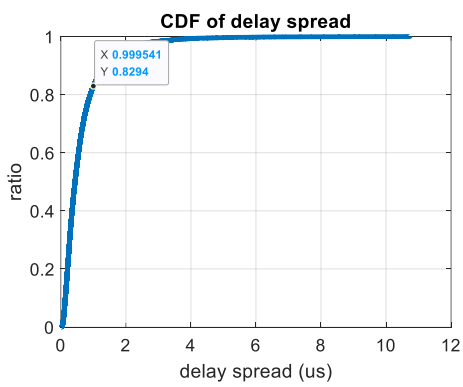

Fig. 1. The empirical delay spread CDF of 10,000 NLoS Urban Macro channel realizations according to the 3D channel model of 5G NR.

Traditional methods for sub-Nyquist signal recovery include non-uniform sampling [19], compressive sensing [20], [21], and iterative shrinkage-thresholding algorithm (ISTA) [22]–[24]. While effective under certain conditions, these approaches assume signal sparsity in a specific domain and may struggle with uniform sampling. Thus, researchers are focusing on deep learning approaches for sub-Nyquist upsampling from uniform samples.

One promising approach is inspired by the super-resolution (SR) techniques for computer vision, which enhance resolution by interpolating low-resolution images [25]. Techniques like the Super-Resolution Convolutional Neural Network (SR-CNN) [26] and hybrid CNN-transformer models [27] have improved image quality. Although SR methods increase data resolution, they rely on structural priors (edges, textures) that are absent in the random CSI data patterns, making them unsuitable for direct application. Some research in communications uses deep learning to recover the beam response map from sparse beam responses, reducing beam search costs in mmWave [28]–[30]. However, these methods assume a reasonably high sampling rate in the beam domain to reflect the true directional power distribution effectively.

While deep learning models in image processing leverage extensive prior information, CSI data lacks such patterns, complicating training. To address this, we propose exploiting UL CSI and leveraging multipath reciprocity to counteract aliasing from undersampling in DL CSI recovery.

B. Contributions

This paper addresses the critical problem of aliasing in CSI feedback caused by low-density CSI-RS pilot placement in current cellular standards. We introduce a novel CSI upsampling framework utilizing UL CSI to mitigate aliasing effects and enhance DL CSI recovery. Our main contributions are as follows:

- **UL Masking Technique:** We develop a low-complexity, rule-based method using the Discrete Fourier Transform (DFT) shifting theorem and multipath reciprocity to design a bandpass filter that suppresses aliasing peaks in the CSI spectrum.
- **SRCsiNet Framework:** We propose a deep learning architecture, SRCsiNet, that extends the UL Masking concept by leveraging the DFT shifting theorem and multipath reciprocity for enhanced CSI upsampling and aliasing suppression.
- **End-to-End Alias Suppression Training:** A SRCsiNet model is trained in an end-to-end manner with a non-aliasing selection map module to generate an adaptive bandpass filter used in the beam-delay domain within a CSI *attention* and refinement module for improved aliasing suppression.
- **Hybrid Integration with ISTA-Net for Non-Uniform Sampling Recovery:** To enhance resilience against non-uniform sampling, we propose a hybrid CSI upsampling approach combining SRCsiNet with the ISTA-Net architecture, enabling efficient aliasing suppression and improved CSI recovery in sparse sampling scenarios.

These contributions bridge critical gaps in the current state of CSI feedback frameworks, paving the way for more accurate and resource-efficient CSI recovery in massive MIMO FDD systems.

II. System Model

A. DL CSI Preprocessing

We consider a single-cell MIMO FDD link where a gNB with N_a antennas serves a plurality of single-antenna UEs. Following 3GPP technical specifications, sparse pilot symbols

(i.e., CSI-RS) are uniformly distributed in the frequency domain for DL channel acquisition. Assume each subband contains N_f subcarriers with a spacing of Δf and a pilot spacing of D_{RS} subcarriers. Adjacent CSI-RSs are separated by $D_{\text{RS}} \cdot \Delta f$ Hz.

We denote $\mathbf{h}_i \in \mathbb{C}^{M_f \times 1}$ as the reference-signal (RS) CSI of the i-th antenna at gNB at M_f pilot (CSI-RS) positions. Let the superscript $(\cdot)^H$ denote the conjugate transpose. By collecting the CSI of each gNB, an RS CSI matrix $\mathbf{H}_{\text{RS}}$ relates to the full DL CSI matrix $\mathbf{H} \in \mathbb{C}^{N_a \times N_f}$ via:

$$\mathbf{H}_{\text{RS}} = \mathbf{H}\mathbf{Q}_{D_{\text{RS}}} = \begin{bmatrix}\mathbf{h}_1 & \mathbf{h}_2 & \cdots & \mathbf{h}_{N_a}\end{bmatrix}^H \in \mathbb{C}^{N_a \times M_f},$$

where

$$\mathbf{Q}_{D_{\text{RS}}} = [\mathbf{e}_1, \mathbf{e}_{1+D_{\text{RS}}}, \ldots, \mathbf{e}_{1+(M_f-1)D_{\text{RS}}}] \in \mathbb{C}^{N_f \times M_f}$$

is a downsampling matrix with pilot rate D_{RS}, and $\mathbf{e}_i \in \mathbb{C}^{N_f}$ is the i-th column vector of an identity matrix of size N_f.

B. DL CSI Feedback

Autoencoder has shown successes for CSI compression. An encoder at UE compresses its estimated DL CSI based on reference signals for UL feedback and a decoder at gNB recovers the CSI according to the feedback from UE. Before compression and after recovery, some works [3], [31] may or may not transform CSI into the domain with sparse features as pre-processing, which usually only pose slight impact. Many have exploited convolutional and fully connected layers to compress and recover the RS CSI via

$$\begin{aligned}\text{Encoder:} \quad & \mathbf{q} = f_{\text{en}}(\mathbf{H}_{\text{RS}} + \mathbf{N}),\\ \text{Decoder:} \quad & \widehat{\mathbf{H}}_{\text{RS}} = f_{\text{de}}(\mathbf{q}).\end{aligned}$$

We note that the size of the codeword $\mathbf{q} \in \mathbb{C}^{\frac{N_a M_f}{CR}}$ for UL feedback is determined by a specific compression ratio CR. We can evaluate the feedback loss by the NMSE of the RS CSI:

$$Loss_{\text{FB}}(\widehat{\mathbf{H}}_{\text{RS}}, \mathbf{H}_{\text{RS}}) = \sum_{d=1}^{D} \frac{\left\|\widehat{\mathbf{H}}_{\text{RS},d} - \mathbf{H}_{\text{RS},d}\right\|_F^2}{\left\|\mathbf{H}_{\text{RS},d}\right\|_F^2},$$

where subscript d denotes the d-th random test.

C. Aliasing Issue

Fig. 2 demonstrates the block diagram of a practical explicit CSI feedback framework. Since UE can only acquire $\mathbf{H}_{\text{RS}}$, gNB needs to upsample $\widehat{\mathbf{H}}_{\text{RS}}$ the actual full DL CSI, denoted as $\mathbf{H}$ after CSI encoding and decoding for precoder design. Thus, our primary interest shifts towards the total discrepancy between the actual full DL CSI, $\mathbf{H}$, and the estimated full DL CSI, denoted as $\widehat{\mathbf{H}}$. The discrepancy is given as follows:

$$Loss = \text{NMSE}(\widehat{\mathbf{H}}, \mathbf{H}) = \sum_{d=1}^{D} \frac{\left\|\widehat{\mathbf{H}}_d - \mathbf{H}_d\right\|_F^2}{\left\|\mathbf{H}_d\right\|_F^2},$$

$$\widehat{\mathbf{H}} = f_{\uparrow}(f_{\text{de}}(f_{\text{en}}(\mathbf{H}_{\text{RS}} + \mathbf{N}))),$$

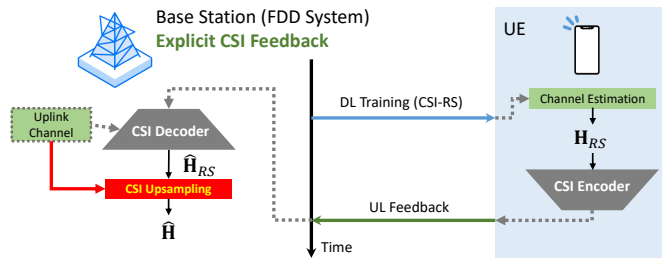

Fig. 2. Block diagram of explicit CSI feedback frameworks. Previous deep learning works on CSI feedbacks neglected the necessity of upsampling RS CSI to full DL CSI or assumed that UE is able to acquire full DL CSI, which is not practical. This work aims to design a CSI upsampler that leverages uplink channels and side information against the aliasing issue.

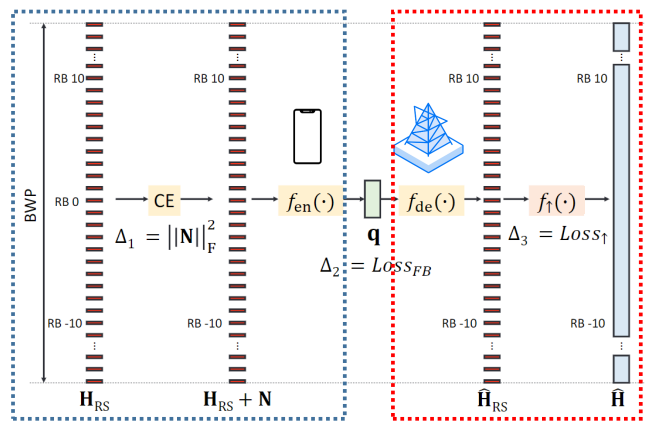

Fig. 3. Illustration of the total discrepancy related to losses at different stages. Δ_1, Δ_2 and Δ_3 denote the distortions from channel estimation at UE side, feedback from UE to gNB, and upsampling, respectively.

where $f_{\uparrow}(\cdot)$ is the upsampling operation and $\widehat{\mathbf{H}} \in \mathbb{C}^{N_a \times N_f}$ is the estimated DL CSI after upsampling/interpolation.

As shown in Fig. 3, the total discrepancy in recovering the full DL CSI, denoted as $Loss$, arises from three main factors: channel estimation (CE) noise $\mathbf{N}$, feedback loss $Loss_{\text{FB}}$, and upsampling/interpolation loss $Loss_{\uparrow}$. The CE loss, resulting from imperfect CE at the UE side, has been effectively addressed by rule-based methods like Least Square (LS) and MMSE estimation [32], as well as advanced learning-based denoising networks [33], [34]. Feedback loss, due to limited CSI feedback, has been extensively explored in existing CSI feedback frameworks [3], [11]. However, there has been less focus on upsampling loss. This loss occurs when interpolating full DL CSIs from a limited number of known estimated RS CSIs. While feedback loss $Loss_{\text{FB}}$ is typically predominant in indoor propagation channels, the insufficient density of current CSI-RS placements means that upsampling loss $Loss_{\uparrow}$ becomes a significant challenge in recovering DL CSIs with large delay spread (i.e., fast-varying in frequency domain).

Prior research often assumes adequate pilot density in the frequency domain for all types of channels. However, the density of pilot placement in CSI-RS, as specified in cellular

network standards [35], falls short for outdoor scenarios, particularly for channels with a high delay spread. This leads to a significant issue: the RS CSI matrix, $\mathbf{H}_{\text{RS}}$, may experience aliasing due to downsampling, rendering it impossible to accurately recover the full DL CSI, $\mathbf{H}$. Let us define the pilot sample rate in frequency as S_{F} and the maximum delay tap as Δt_{max} seconds. If $\frac{1}{2S_{\text{F}}} \leq \Delta t_{\text{max}}$, the channels captured from CSI-RS are considered to be aliased signals. Generally, recovering aliased signals (i.e., aliased downsampled (DS) CSI) to their original form (i.e., full CSI) is not feasible.

To give some realistic examples, based on the highest density of placement of CSI-RS, which is 1 per 12 subcarriers of 15 kHz, the frequency sampling interval is 180 kHz. According to the Nyquist theorem, the maximum measurable delay is half the inverse of the frequency interval, i.e., $\frac{1}{2\cdot 180\text{ kHz}} = 2.778$ microseconds. Consequently, any path delay greater than the maximum measurable delay will wrap around into the low delay region (i.e., so-called aliasing effect). Specifically, once the delay spread exceeds 1.4 microseconds, aliasing effects are inevitable regardless of the mean excess delay. If the mean excess delay is significant, aliasing can also occur even if the delay spread is less than 1000 nanoseconds. In practical field tests [15], [16], some research findings corroborate our points by demonstrating that, in the sub-6 GHz band, the delay spread of some measured channels can exceed 1000 nanoseconds. Additionally, according to the 3D channel model study for 5G NR [17], the delay spread of about 20% of NLoS Urban Macro channels is greater than 1 microsecond, as illustrated in Fig. 1.

However, if the DS signals satisfy certain constraints, we may recover the full CSI with aids of side information, which will be introduced in the following sections. Previous studies often assume an overly idealistic approach to upsampling/interpolation, which can be a *critical operation* in channels with a large delay spread, and results in a bottleneck in reducing the total discrepancy[1]. To enhance the overall performance, our focus should shift to improving this critical operation rather than the other two.

III. UL-CSI AIDED UPSAMPLIGN WITH ALIASING SUPPRESSION

A. CSI Upsampling with Side Information

For an arbitrary channel $\mathbf{H} \in \mathbb{C}^{N_a \times N_f}$ in frequency domain and its DS version $\mathbf{H}_{\text{RS}} = \mathbf{H}\mathbf{Q}_{D_{\text{RS}}} \in \mathbb{C}^{N_a \times M_f}$ by a factor of D_{RS}. If we upsample the $\mathbf{H}_{\text{RS}}$ by inserting $D_{\text{RS}} - 1$ zeros between any two consecutive samples along frequency domain, we have

$$\mathbf{H}_{\text{DS}}[:, j] = \begin{cases} \mathbf{H}[:, j], & \forall j \in \Psi_{\text{RS}}, \\ \mathbf{0}, & \forall j \notin \Psi_{\text{RS}}, \end{cases} \tag{1}$$

where $\Psi_{\text{RS}} = \{0, D_{\text{RS}}, ..., (M_f - 1)D_{\text{RS}}\}$ is a downsampling index set. Note that $\mathbf{H}_{\text{DS}}$ consists of the entries of $\mathbf{H}_{\text{RS}}$ at frequencies with pilots and zeros elsewhere. By DFT/IDFT transformation, the full and DS DL CSI in beam-delay (BD) domain can be obtained as follows:

$$\mathbf{H}_{\text{BD}} = \mathbf{F}_{\text{AB}}\mathbf{H}\mathbf{F}_{\text{FD}} \in \mathbb{C}^{N_a \times N_f},$$

$$\mathbf{H}_{\text{DS,BD}} = \mathbf{F}_{\text{AB}}\mathbf{H}_{\text{DS}}\mathbf{F}_{\text{FD}} \in \mathbb{C}^{N_a \times N_f}, \tag{2}$$

where $\mathbf{F}_{\text{AB}} \in \mathbb{C}^{N_a \times N_a}$ and $\mathbf{F}_{\text{FD}} \in \mathbb{C}^{N_f \times N_f}$ are DFT and IDFT transformation matrices, respectively. The subscripts AB and FD denote the transformation from antenna/frequency to beam/delay domains, respectively. Note that we use subscript BD, AD, AF to denote CSI in beam-delay, angle-delay, and angle-frequency domains, respectively. We use no subscript to denote CSI in the orignal domain which is antenna-frequency domain.

Given the *DFT shifting theorem* [36], when a time-domain signal is uniformly downsampled by a factor of D_{RS}, its frequency representation is folded D_{RS} times. Applying this concept, when we uniformly downsample $\mathbf{H}$ and subsequently perform an DFT/IDFT transformations in antenna and frequency domains, respectively, we obtain $\mathbf{H}_{\text{DS,BD}}$, which represents $\mathbf{H}_{\text{BD}}$ folded in the delay domain. It is important to note that this folding occurs regardless of whether the matrix is in the antenna or beam domain, as the downsampling is not performed in the antenna domain. This results in the following relationship between the full and downsampled DL CSIs:

$$\mathbf{H}_{\text{DS,BD}}[i, j] = \begin{cases} \dfrac{\mathbf{H}_{\text{BD}}[i, j] + \mathbf{H}_{\text{BD}}[i, j + M_f] + \\ ... + \mathbf{H}_{\text{BD}}[i, j + M_f(D_{\text{RS}} - 1)]}{D_{\text{RS}}}, \forall 0 \leq j < M_f \\ \mathbf{H}_{\text{DS,BD}}[i, \text{mod}(j, M_f)], \text{otherwise} \end{cases}. \tag{3}$$

Note that $\mathbf{H}_{\text{DS,BD}}$ is periodic in the delay domain with a period of $M_f = N_f/D_{\text{RS}}$. If $\mathbf{H}_{\text{BD}}[i, j] \neq 0$ for any $j > M_f$, we can say that the aliasing effect occurs and it cannot be recovered to the original version $\mathbf{H}$ in general cases since we can only measure $\mathbf{H}_{\text{DS,BD}}$, the sum of the multipaths. However, since $\mathbf{H}_{\text{DS,BD}}$ is periodic in the delay domain with a period of M_f, which matches the wrapped-around effect due to downsampling, the IDFT transformation *unwraps* the delay bins of $\mathbf{H}_{\text{BD}}$ to the original delay positions. Thus, $\mathbf{H}$ can be recovered if $\mathbf{H}_{\text{BD}}[i, j]$ in the delay domain satisfies the two requirements shown below:

- **Bin Isolation Property**: for any non-zero $\mathbf{H}_{\text{DS,BD}}[i, j]$ in Eq.(3), only one from the D_{RS} aliased copies $\mathbf{H}_{\text{BD}}[i, j], \mathbf{H}_{\text{BD}}[i, j + N_f/D_{\text{RS}}], ..., \mathbf{H}_{\text{BD}}[i, j + N_f(D_{\text{RS}} - 1)/D_{\text{RS}}]$ is non-zero. Namely, the delay bins (i.e., $\mathbf{H}_{\text{BD}}[i, j], j > M_f$) and the low-delay bin (i.e., $\mathbf{H}_{\text{BD}}[i, j], j \leq M_f$) are isolated after wrapped-around in its DS version. If the bin isolation property holds, each non-zero DS signal $\mathbf{H}_{\text{DS,BD}}[i, j]$ in delay domain maps to a scaled unique delay bin in the original signal (i.e.,

[1]As the three operations (estimation, feedback, and interpolation) are sequential, the one causing the largest loss becomes the bottleneck in reducing the total discrepancy. This operation is termed the critical operation.

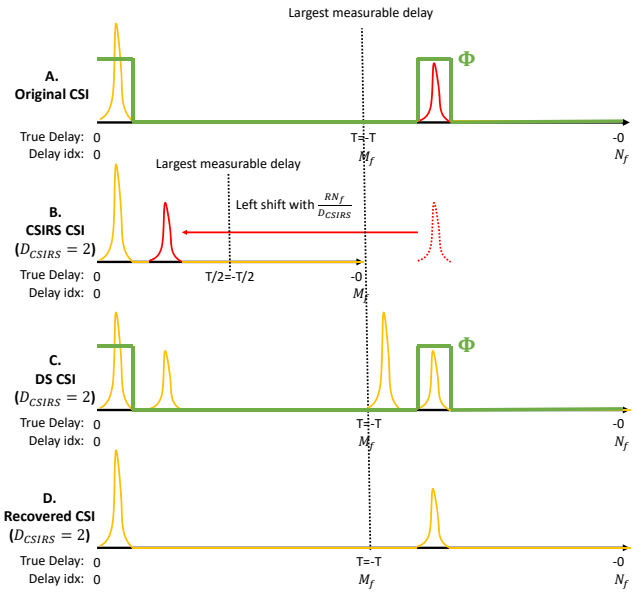

Fig. 4. Illustration of CSI upsampling with side information. (A) shows the original CSI magnitude in delay domain. (B) demonstrates the CSIRS CSI magnitude in delay domain when $D_{\text{RS}} = 2$. We can find that the high negative delay peak wraps around ($R = 1$) into the low delay region, leading aliasing effect. (C) shows the DS CSI magnitude in delay domain by inserting zero inbetween samples of CSIRS CSI in frequency domain. The green curve represents an ideal binary bandpass filter $\mathbf{\Phi}$ to be the side information. (D) is the resulting DL CSI magnitude in delay domain after applying the binary bandpass filter $\mathbf{\Phi}$.

$\mathbf{H}_{\text{DS,BD}}[i,j] = \mathbf{H}_{\text{BD}}[i,n_k]/D_{\text{RS}}$). Note that n_k can only be j, $j+M_f$,..., or $j+(D_{\text{RS}}-1)M_f$.

- **Knowledge of bin locations**: we have the perfect knowledge map $\mathbf{\Phi} \in \mathbb{C}^{N_a \times N_f}$ with ones at the positions with non-zero values in the the full CSI matrix $\mathbf{H}_{\text{BD}}[i,j]$ and zeros elsewhere.

Fig. 4 shows a simple illustration for the single antenna case with the intermediate results of the proposed CSI upsampling approach using the bin location information. If the full CSI matrix $\mathbf{H}_{\text{BD}}$ satisfies the above two requirements, $\mathbf{H}_{\text{BD}}$ can be ideally obtained by

$$\widehat{\mathbf{H}}_{\text{BD}} = D_{\text{RS}}\mathbf{\Phi} \circ \mathbf{H}_{\text{DS,BD}} \approx \mathbf{H}_{\text{BD}}.$$

Note that $\circ$ denotes the element-wise product operation. $\mathbf{\Phi}$ acts like a bandpass filter in BD domain. Although the two requirements are ideal, they lead us to a rationale to deal with aliasing problems. That is, to deal with sparse signals, we can suppress aliasing peaks with the knowledge of the non-zero bin locations as a *bandpass filter*. In practice, DL CSI is somehow sparse so that a *quasi bin isolation property* can hold. As for the knowledge of bin locations of DL CSI, we can estimate it according to UL CSI at base stations.

B. Multipath Reciprocity

Typically, acquiring the exact delay bin location information without the original DL CSI, denoted as $\mathbf{H}_{\text{BD}}$, is challenging. However, in communications systems, the magnitudes of DL CSI in the BD domain $\mathbf{H}_{\text{BD}}$ is often closely correlated with

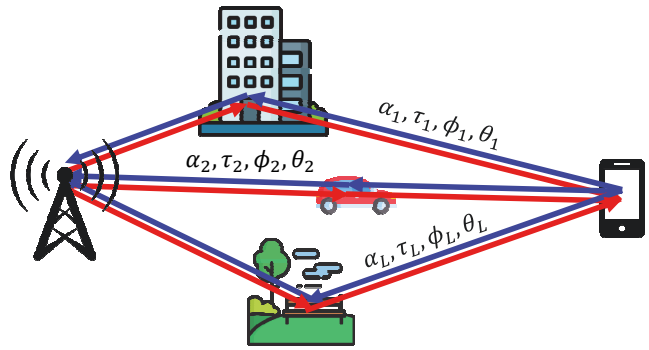

Fig. 5. Illustration of multipath reciprocity between UL and DL propagation channels.

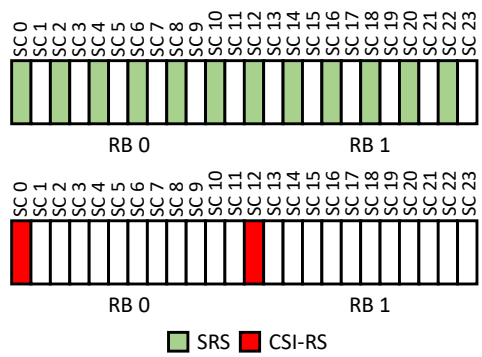

Fig. 6. Comparison of SRS and CSI-RS placement density.

the magnitudes of UL CSI in BD domain $\mathbf{H}_{\text{UL,BD}}$, which is readily available at base stations. Although DL and UL CSIs do not exhibit full correlation in FDD wireless systems, as illustrated in Fig. 5, they often share similar large-scale multipath geometries (i.e., since the paths from/to gNB are bidirectional, the delays and angles UL/DL paths should be nearly identical to each other). This multipath reciprocity results in comparable delay and angle profiles, a finding supported by field tests and mathematical analysis [37]–[39]. Therefore, UL CSI in the BD domain is typically considered a reliable estimate for the AD profiles of DL CSI. Owing to the relatively high pilot placement density in UL CSI, there are no aliasing effects, allowing for the design of a bandpass filter to mitigate aliasing effects in DL CSIs.

In modern communication systems, as depicted in Fig. 6, the pilot placement density in the frequency domain of the Sounding Reference Signal (SRS) is much higher (every two subcarriers) compared to that of CSI-RS (every 12 subcarriers). Consequently, the maximum non-aliasing delay (i.e., measurable delay) of UL CSI is approximately six times greater than that of DL CSI, virtually eliminating aliasing effects in UL CSIs. Based on the principle of multipath reciprocity, this work proposes designing the bandpass filter $\mathbf{\Phi}$ using UL CSI information.

C. UL Masking: UL-Assisted CSI Upsampling with Aliasing Suppression

Assume that we have perfect UL CSI $\mathbf{H}_{\text{UL}}$. According to the multipath reciprocity between UL and DL CSIs, we can design a two-dimensional bandpass filter based on the UL CSI magnitude in BD domains as follows:

$$\mathbf{\Phi}_{\text{UL}}[i,j] = \begin{cases} 0, & |\mathbf{H}_{\text{UL,BD}}[i,j]| < T, \\ 1, & |\mathbf{H}_{\text{UL,BD}}[i,j]| \geq T, \end{cases}$$

$$\mathbf{H}_{\text{UL,BD}} = \mathbf{F}_{\text{AB}}\mathbf{H}_{\text{UL}}\mathbf{F}_{\text{FD}} \in \mathbb{C}^{N_a \times N_f},$$

where we set $T = R \cdot \sqrt{P}$ and P is the average power of $\mathbf{H}_{\text{UL,BD}}$. We next can estimate the BD domain DL CSI by

$$\widehat{\mathbf{H}}_{\text{BD}} = \mathbf{\Phi}_{\text{UL}} \circ \mathbf{H}_{\text{DS,BD}}.$$

Leveraging multipath reciprocity, the filter can suppress aliased copies if we establish an appropriate threshold T to define the pass band/region in the delay and angle domains. In practice, we perform a line search over all possible R values in the training dataset before using the chosen R for inference in real time. An adaptive tracking algorithm could be employed to smooth or predict R for improving filter design. However, finding a universal hard threshold T for all types of CSI remains challenging due to imperfect multipath reciprocity. Applying a "soft" threshold map offers more flexibility, allowing partial dependency on multipath components. Inspired by this insight, in the following section, we explore the use of a deep learning model to design a soft bandpass filter based on UL CSI.

IV. Physic-inspired AI-driven Aliasing Suppression

Previous works [7], [9], [40] have been successfully applied to in CSI compression and recovery. Enough pilot sampling rate was usually assumed. In fact, following the 3GPP 5G NR standard [35], UEs estimate the channels from CSI-RS and send channel state feedback. However, the frequency density of CSI-RS is not sufficient to capture the fast channel variation along frequency domain. Even if a perfect CSI feedback is achieved, the aliasing loss due to downsampling is theoretically not possible to be recovered.

A. Model Architecture

There are plenty of successful network architecture which can enhance image details while maintaining visual fidelity after SR operation. In a sense of information theory, the model learns prior information from the training data to fill the information gap between the target and desired images. There are lots of common features in images such as facial features, colors textures, edges and shapes. For example, as long as the deep learning model can recognize a specific patch as a face, it can largely lower the uncertainty to upsample the LR images since there exists nothing else except facial features. However, unlike SR task in computer vision, the details of CSIs are random and difficult to learn as prior information stored in the deep learning model. To fill the information gap, we propose to utilize UL CSI information by exploiting multipath reciprocity against aliasing effects due to an insufficient pilot sampling rate.

This section introduces a general learning framework designed to effectively upsample LR tensors into SR equivalents. This process is akin to the SR challenge in computer vision, where numerous successful networks [26], [27], [41] have been developed to enhance image details while preserving visual fidelity after SR operation. From the perspective of information theory , the model employs prior knowledge obtained from training data to fill the gap between actual and desired images. Certain image features, including facial characteristics, colors, textures, edges, and shapes, are common across various images. These features are retained as prior knowledge within the model, ready to be utilized as necessary to aid in image processing tasks. For instance, if a deep learning model identifies a particular segment as part of a face, it significantly reduces the uncertainty involved in upscaling LR images, since the expected features are confined to those associated with faces.

However, unlike the SR task in computer vision, the intricacies of CSI are random and challenging to learn as pre-existing information within a deep learning model. To overcome this information gap, we propose leveraging UL CSI data, exploiting the principle of multipath reciprocity to counteract the aliasing effects stemming from an inadequate pilot sampling rate. Fig. 7 gives a high-level understanding of the proposed architecture. This framework is designed to be deployed at base stations and consists of three modules: a) non-aliasing selection map generation, b) true peak recovery, and c) CSI attention and refinement which are described in detail as follows:

1) True Peak Recovery

This module aims to upsample LR DL CSIs by inserting zeros and transform them into the beam and delay domains. By doing so, we can have a DL CSI map in BD domain which is periodic in delay domain. According to the DFT shifting invariance property, we can map the aliasing delay bins to its original positions by inserting $D-1$ zeros in between samples. On the other hand, this will also lead to more false peaks in the repetition map at the false delay positions. To implement, we basically follow Eqs. (1) and (2) to generate the desired repetition map $\mathbf{H}_{\text{BD,DS}}$. We describe these operations as a linear function $f_{\text{TPR}}(\cdot)$ such that $\mathbf{H}_{\text{BD,DS}} = f_{\text{TPR}}(\mathbf{H}_{\text{RS}})$.

2) Non-aliasing Selection Map Generation (Bandpass Filter Design)

This module aims to generate a bandpass filter in the BD domain which can suppress aliasing peaks at wrong delay positions. Regarding the multipath reciprocity, we can reply on UL CSI to infer where the true peaks are. Instead of using a rule-based approach mentioned in the previous section, we adopt a neural network to design a bandpass filter. We first transform the HR UL CSI into BD domain as $\mathbf{H}_{\text{BD,UL}}$

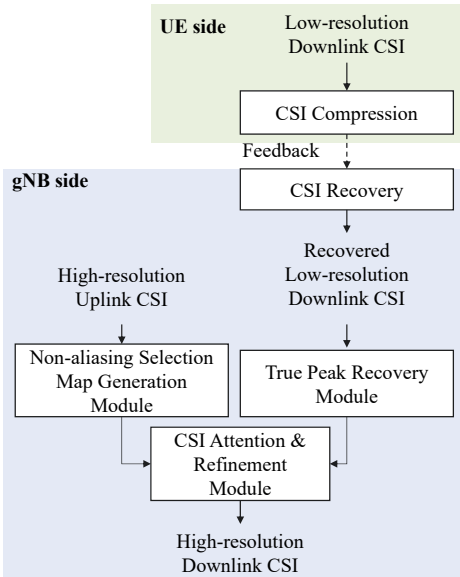

Fig. 7. General architecture of the proposed physic-inspired AI-driven aliasing suppression framework. This framework consists of two parts. The first part is CSI compression and recovery which are deployed at UE and base station sides, respectively. The other part is the SR operation for the LR CSIs.

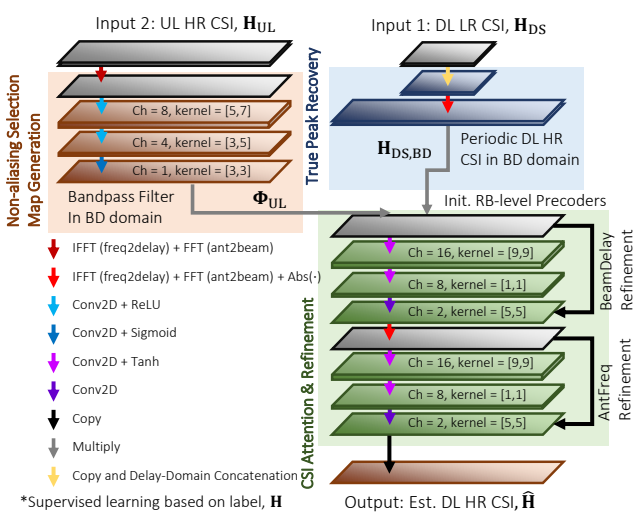

Fig. 8. Network architecture of SRCsiNet. It consists of three modules: 1) Non-aliasing selection map generation, 2) True peak generation and 3) CSI attention and refinement.

with the same size of the matrix $\mathbf{H}_{\mathrm{BD,DS}}$ to be filtered. We then feed $\mathbf{H}_{\mathrm{BD,UL}}$ into three convolutional layers with two ReLU activations at the outputs of the first two convolutional layers. We then utilize a sigmoid function as the last activation function to output the bandpass filter $\mathbf{\Phi}_{\mathrm{UL}}$ since it perfectly matches the soft filtering purpose (i.e., model cannot only yield zeros to suppress aliasing delay positions and ones elsewhere, but also yield values between 0 and 1 to represent the model uncertainty and provide flexibility). We called it as Bandpass Filter Design (BFD) Block. For brevity, we can express the output of the branch of the model as

$$\mathbf{\Phi}_{\mathrm{UL}} = f_{\mathrm{BFD}}(\mathbf{H}_{\mathrm{UL}}). \tag{4}$$

3) *CSI Attention and Refinement*

This module aims to filter out the aliasing peaks and do refinement to generate the final DL CSI estimates which can be expressed as $\widehat{\mathbf{H}} = f_{\mathrm{AR}}(\mathbf{\Phi}_{\mathrm{UL}} \circ \mathbf{H}_{\mathrm{BD,DS}})$. The function $f_{\mathrm{AR}}(\cdot)$ aims to further refine and smooth the filtered result which may have some artifacts due to the imperfect bandpass filter $\mathbf{\Phi}_{\mathrm{UL}}$ and the overlapped delay bins in $\mathbf{H}_{\mathrm{BD,DS}}$. We apply two residual blocks with SRCNN block [26] as the backbone to refine the estimate first in BD domain and then in AF domain.

B. *Loss Function Design*

This network aims to minimize the upsampling loss $Loss_{\uparrow}$ which is defined as

$$\begin{aligned} Loss_{\uparrow}(\Theta_{\mathrm{BFD}}, \Theta_{\mathrm{AR}}) &= \frac{1}{D}\sum_{d}^{D}\left\|\widehat{\mathbf{H}}_d - \mathbf{H}_d\right\|_F^2, \\ &= \frac{1}{D}\sum_{d}^{D}\left\|f_{\mathrm{AR}}(\mathbf{\Phi}_{\mathrm{UL},d} \circ \mathbf{H}_{\mathrm{BD,DS}}) - \mathbf{H}_d\right\|_F^2, \\ &= \frac{1}{D}\sum_{d}^{D}\left\|f_{\mathrm{AR}}(f_{\mathrm{BFD}}(\mathbf{H}_{\mathrm{UL},d}) \circ \mathbf{H}_{\mathrm{BD,DS}}) - \mathbf{H}_d\right\|_F^2, \end{aligned}$$

where Θ_{BFD} and Θ_{AR} are trainable parameters of the functions $f_{\mathrm{BFD}}(\cdot)$ and $f_{\mathrm{AR}}(\cdot)$, respectively. It is important to mention that minimizing the MSE loss plays a crucial role in guiding the non-aliasing selection map generation module to design a high-quality bandpass filter. The output of the true peak recovery module may contain true peaks but can also include aliasing peaks. Without a well-designed bandpass filter, the upper part of SRCsiNet may pass a significant amount of irrelevant and ambiguous information—such as aliasing peaks that resemble true peaks but have incorrect delay positions—to the CSI attention and refinement module, leading to a higher MSE loss. Therefore, to effectively minimize MSE loss, it is essential to have a high-quality bandpass filter.

C. *Limitations and Failure Scenarios*

As mentioned in Section III.A, the full DL CSI $\mathbf{H}$ can be recovered if $\mathbf{H}_{\mathrm{BD}}$ satisfies two requirements: bin sparsity and knowledge of bin locations. Low sparsity tends to cause overlapped delay bins, which cannot be separated. Even if channel sparsity is high but the magnitude correlation is low, the proposed approaches would generate a poor-quality mask that cannot correctly mitigate aliasing delay bins. Yet, considering the propagation model and path reciprocity, the two requirements are true for most cases. If the two requirements are not met, in fact, there is little else one can do from information theoretic perspective.

V. Efficient Channel State Feedback with Aliasing Suppression from Non-uniform Sampling

The true delay position information can significantly improve the CSI recovery for high-delay scenarios. In the perspective of the information theory, if we can increase the mutual information between the input and the desired output, we can further improve the CSI recovery accuracy.

According to the 3GPP 5G-NR standards [35], the primary and secondary synchronization signals (PSS and SSS) play crucial roles in cell identification and frame synchronization, appearing periodically every 25 subframes (approximately 25ms) and spanning 64-128 subcarriers in bandwidth. Beyond these primary functions, as depicted in Fig. 9, UEs can also utilize PSS and SSS to estimate DL CSI, treating these signals as *virtual pilots* for DL CSI acquisition. Furthermore, the Physical Broadcast Channel (PBCH), instrumental for broadcasting system information and aiding UEs in network access, also contributes to DL CSI estimation by UEs, acting as additional virtual pilots. This dense placement of virtual pilots (SSS, PSS, and PBCH) aids in detecting multipath effects with large delays, which CSI-RS might miss, despite the mismatch in bandwidth coverage with the bandwidth part (BWP) designated for UEs.

In an ideal scenario, combining the channels from sparse uniform pilots (CSI-RS) with those from dense virtual pilots would enable us to harness the strengths of both pilot types, leading to more accurate CSI recovery. However, the effectiveness of our proposed architecture, SRCsiNet, hinges on maintaining a uniform sampling relationship between input and output to exploit the Inverse Discrete Fourier Transform (IDFT) shifting invariance property.

This section will introduce the integration of a compressive sensing-based deep learning model into SRCsiNet, to address the challenges posed by a non-uniform pilot setup while effectively employing a bandpass filter. We will begin by outlining the compressive sensing-based CSI upsampling method, followed by an introduction to a novel framework, SRISTA-Net.

A. Compressive sensing based CSI upsampling

As illustrated in Fig. 9, considering the extra subcarrier-level DL CSIs, we can express the non-uniform RS CSI, termed as LR DL CSI for simplicity, as

$$\mathbf{H}_{\text{LR}}[i,j] = \begin{cases} \mathbf{H}[i,j], \forall j \in \Psi_P, \\ 0, \forall j \notin \Psi_P, \end{cases} \tag{5}$$

where $\Psi_P = \Psi_{\text{RS}} \cup \Psi_{\text{ex}}$ is the union of Ψ_{RS} and $\Psi_{\text{ex}} = \{I, I+1, ..., I+P-1\}$ with I being the smallest subcarrier index in SSS, PSS or PBCH. Ψ_{ex} is the index set of the consecutive pilots with size of P. We can reformulate the LR DL CSI based on the full AD DL CSI as

$$\mathbf{H}_{\text{LR}} = \mathbf{H}\mathbf{I}[:, \Phi_{\text{P}}] = \mathbf{H}\mathbf{F}_{\text{FD}}\mathbf{F}_{\text{FD}}^{H}\mathbf{I}[:, \Phi_{\text{P}}] \tag{6}$$

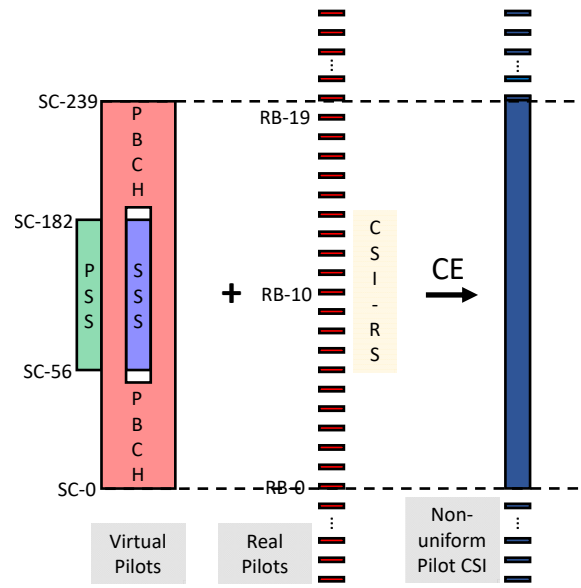

Fig. 9. Illustration of virtual pilots (i.e., PBCH, SSS and PSS) and non-uniform RS CSI. With the sparse uniform pilots (CSI-RS) and the dense virtual pilots, we can have an effective non-uniform DL CSI.

where $\widetilde{\mathbf{F}}_{\text{FD}} = \mathbf{F}_{\text{FD}}[:, \Phi_{\text{P}}] \in \mathbb{C}^{N_f \times |\Phi_{\text{P}}|}$ is the trimmed DFT transformation matrix.

Mathematically, the goal of compressive sensing reconstruction is to infer the original signal $\mathbf{x} \in \mathbb{C}^N$ from a low-dimensional measurement $\mathbf{y} = \mathbf{\Phi}\mathbf{x} \in \mathbb{C}^M$, where $M \ll N$. By transposing Eq.(6), we have an exact projection of the problem of interest to a compressive sensing reconstruction problem (i.e., $\mathbf{y} = \mathbf{H}_{\text{LR}}[i,:]^T$, $\mathbf{\Phi} = \widetilde{\mathbf{F}}_{\text{FD}}^T$, $\mathbf{x} = \mathbf{H}_{\text{AD}}[i,:]^T$ where $i = 1, ..., N_a$). This inversion is typically ill-posed problem. However, it can be solved by compressive sensing reconstruction since the sparsity of the original CSIs regularizes the possible outputs.

B. ISTA-Net Framework

Previous works have proposed a deep unfolding approach called ISTA-Net [23]. The basic idea of ISTA-Net is to map the previous Iterative Soft-Thresholding Algorithm (ISTA) [22] approach updating steps to a deep learning network. This architecture consists of a fixed number of phases, each of the phase performs one iteration in classic ISTA algorithm.

Fig. 10 shows the deep learning network of the ISTA-Net. For each phase in ISTA-Net, it consists of two modules, namely the $\mathbf{r}^{(k)}$ **module** and the $\mathbf{x}^{(k)}$ **module**. The following items describe the operation in k-th phase as follows:

- $\mathbf{r}^{(k)}$ **Module**: This aims to produce the intermediate result which is the same as the ISTA algorithm. This step is to optimize the channel fidelity $\left\| \widetilde{\mathbf{F}}_{\text{FD}}^T \mathbf{x}^{(k-1)} - \mathbf{H}_{\text{LR}}[i,:]^T \right\|_2^2$. To maintain the ISTA architecture while increasing the channel similarity, a trainable step size $\rho^{(k)}$ to vary across different phases is adopted so that the output of this module with input $\mathbf{x}^{(k-1)}$ for i-th antenna can be represented as:

$$\mathbf{r}^{(k)} = \mathbf{x}^{(k-1)} - \rho^{(k)}\widetilde{\mathbf{F}}_{\text{FD}}(\widetilde{\mathbf{F}}_{\text{FD}}^T\mathbf{x}^{(k-1)} - \mathbf{H}_{\text{LR}}[i,:]^T). \quad (7)$$

- $\mathbf{x}^{(k)}$ **Module**: It aims to compute $\mathbf{x}^{(k)}$ according to the intermediate result $\mathbf{r}^{(k)}$, which is given by

$$\mathbf{x}^{(k)} = \widetilde{\mathcal{F}}^{(k)}(soft(\mathcal{F}^{(k)}(\mathbf{r}^k), \theta^{(k)})), \quad (8)$$

where a pair of functions $\mathcal{F}^{(k)}$ and $\widetilde{\mathcal{F}}^{(k)}$ which are inverse of each other such that $\widetilde{\mathcal{F}}^{(k)}(\mathcal{F}^{(k)}(\cdot)) = \mathcal{I}(\cdot)$ with $\mathcal{I}(\cdot)$ being an identity function. Such a constraint on $\mathcal{F}^{(k)}$ and $\widetilde{\mathcal{F}}^{(k)}$ is called symmetry constraint.

C. SRISTA-Net Framework

The ISTA-Net can deal with non-uniform sampling but cannot exploit side information. Thus, in this subsection, we propose a new framework which combines ISTA-Net and the proposed SRCsiNet for exploiting the advantages of the two networks, which is termed as *SRISTA-Net*.

Fig. 11 shows the deep learning network of the proposed network SRISTA-Net. We incorporate the SRCsiNet features into ISTA-Net by appending an additional block, Reciprocity Assisting (RA) Block, before the $\mathbf{r}^{(k)}$ module. This block aims to suppress the aliasing effects of the input $\mathbf{x}^{(k-1)}$ prior to solving the proximal mapping by applying the UL CSI assisted bandpass filter according to multipath reciprocity. We feed the magnitude of UL CSI $\mathbf{H}_{\text{UL,BD}}$ in the BD domain into two convolutional layers with ReLU and sigmoid functions, respectively, to obtain a bandpass filter $\mathbf{\Phi}_{\text{UL}}$.

Intuitively, for early phases, the model tends to heavily rely on UL CSI information and vice versa. Therefore, we design a weight matrix $\mathbf{W}^{(k)} \in \mathbb{C}^{N_a \times N_f}$ to adjust the dependency to the UL CSI at the k-th phase. We can rewrite the output of RA block as

$$\mathcal{R}^{(k)}(\mathbf{r}^{(k)}, \mathbf{H}_{\text{UL,BD}}) = \mathbf{W}^{(k)} \circ \mathbf{\Phi}_{\text{UL}} \circ \mathbf{r}_{\text{BD}}^{(k)} + (1 - \mathbf{W}^{(k)}) \circ \mathbf{r}_{\text{BD}}^{(k)}, \quad (9)$$

where $\mathbf{r}_{\text{BD}}^{(k)}$ is the $\mathbf{r}^{(k)}$ after transformation to BD domain. We then feed the output into the $\mathbf{x}^{(k)}$ module in ISTA-Net for minimizing the L1-norm constraints.

D. Loss Function Design

Given the training data pair $\{(\mathbf{H}_{\text{LR}}, \mathbf{H}_{\text{UL,BD}}, \mathbf{H})\}_{d=1}^{D}$, SRISTA-Net first transform $\mathbf{H}_{\text{LR}}$ into its AD version $\mathbf{H}_{\text{LR,AD}}$ as input and feed in the UL CSI information $\mathbf{H}_{\text{UL,BD}}$ in each phase to generate the output $\mathbf{x}_d^{(K)}$. Note that $\mathbf{H}_d$, $\mathbf{x}_d^{(k)}$ and $\mathbf{r}_d^{(k)}$ are all in the AF domain. To reduce the discrepancy between $\mathbf{H}_d$ and $\mathbf{x}^{(K)_d}$ while maintaining the symmetry constraint $\widetilde{\mathcal{F}}^{(k)}(\mathcal{F}^{(k)}(\cdot)) = \mathcal{I}(\cdot), \forall k = 1, ..., K$, we design the following loss function:

$$\mathcal{L}_{\text{all}}(\Theta) = \mathcal{L}_{\text{discrepancy}} + \gamma\mathcal{L}_{\text{symmetry}}, \quad (10)$$

$$\mathcal{L}_{\text{discrepancy}} = \sum_{d=1}^{D}\left\|\mathbf{x}_d^{(K)} - \mathbf{H}_d\right\|_2^2, \quad (11)$$

$$\mathcal{L}_{\text{symmetry}} = \sum_{d=1}^{D}\sum_{k=1}^{K}\left\|\widetilde{\mathcal{F}}^{(k)}(\mathcal{F}^{(k)}(\mathbf{q}_d^{(k)})) - \mathbf{q}_d^{(k)}\right\|_2^2, \quad (12)$$

where $\mathbf{q}_d^{(k)} = \mathcal{R}^{(k)}(\mathbf{r}^{(k)}, \mathbf{H}_{\text{UL,BD}})$ is the output of the RA block at the k-th phase. D, K and γ are the total number of training data size, the total number of SRISTA-Net phases, and the regularization parameter, respectively. In this paper, we follow the original manuscript of ISTA-Net for the value of $\gamma = 0.01$.

E. Initialization

Like traditional iterative compressive sensing reconstruction, the proposed approach requires an initialization denoted by $\mathbf{x}^{(0)}$ as illustrated in Fig. 11. From Eq.(6), we know $\mathbf{H}_{\text{LR}}[i,:]^T = \widetilde{\mathbf{F}}_{\text{FD}}^T\mathbf{H}_{\text{AD}}[i,:]^T, \forall i = 1, ..., N_a$. We take the LS solution to this problem for initialization such that

$$\mathbf{x}^{(0)} = \widetilde{\mathbf{F}}_{\text{FD}}^*(\widetilde{\mathbf{F}}_{\text{FD}}^T\widetilde{\mathbf{F}}_{\text{FD}}^*)^{-1}\mathbf{H}_{\text{LR}}^T \quad (13)$$

To clarify the complex operations of SRISTA-Net, Alg. 1 shows the pseudo code of SRISTA-Net Framework.

Algorithm 1 SRISTA-Net Framework

Require: $\mathbf{H}_{\text{LR}}$, $\mathbf{H}_{\text{UL,BD}}$, K, γ
Ensure: Recovered DL CSI $\mathbf{x}^{(K)}$ in AD domain
Initialize: $\mathbf{x}^{(0)} = \widetilde{\mathbf{F}}_{\text{FD}}^*(\widetilde{\mathbf{F}}_{\text{FD}}^T\widetilde{\mathbf{F}}_{\text{FD}}^*)^{-1}\mathbf{H}_{\text{LR}}^T$
for $k = 1$ to K **do**
  ISTA-Net r **Module:**
  $\mathbf{r}^{(k)} = \mathbf{x}^{(k-1)} - \rho^{(k)}\widetilde{\mathbf{F}}_{\text{FD}}(\widetilde{\mathbf{F}}_{\text{FD}}^T\mathbf{x}^{(k-1)} - \mathbf{H}_{\text{LR}}^T)$
  RA Block:
  $\mathbf{\Phi}_{\text{UL}} = f_{\text{BFD}}(\mathbf{H}_{\text{UL,BD}})$
  $\mathbf{W}^{(k)} = \text{Sigmoid}(\mathbf{W}_1 * \text{MaxPool}(\text{RuLU}(\text{Conv2D}(\text{RuLU}(\text{Conv2D}((\mathbf{H}_{\text{UL,BD}}))))))))$
  $\mathbf{r}_{\text{BD}}^{(k)} = \mathbf{F}_{\text{BA}}\mathbf{x}^{(k-1)}$
  $\mathbf{r}^{(k)} = \mathbf{F}_{\text{BA}}^H(\mathbf{W}^{(k)} \circ \mathbf{\Phi}_{\text{UL}} \circ \mathbf{r}_{\text{BD}}^{(k)} + (1 - \mathbf{W}^{(k)}) \circ \mathbf{r}_{\text{BD}}^{(k)})$
  ISTA-Net x **Module:**
  $\mathbf{x}^{(k)} = \widetilde{\mathcal{F}}^{(k)}(\text{soft}(\mathcal{F}^{(k)}(\mathbf{r}^{(k)}), \theta^{(k)}))$
end for
Loss Function:
$\mathcal{L}_{\text{all}}(\Theta) = \mathcal{L}_{\text{discrepancy}} + \gamma\mathcal{L}_{\text{symmetry}}$
$\mathcal{L}_{\text{discrepancy}} = \sum_{d=1}^{D}\|\mathbf{x}_d^{(K)} - \mathbf{H}_d\|_2^2$
$\mathcal{L}_{\text{symmetry}} = \sum_{d=1}^{D}\sum_{k=1}^{K}\|\widetilde{\mathcal{F}}^{(k)}(\mathcal{F}^{(k)}(\mathbf{q}_d^{(k)})) - \mathbf{q}_d^{(k)}\|_2^2$

VI. Experimental Evaluations

A. Experiment Setup

Tests were focused on outdoor channels using widely used channel model software, QuaDriGa. The simulator considers a gNB with an 8×4 UPA and 32-element ULA serving single-antenna UEs, respectively, with half-wavelength uniform spacing. 2000 UEs uniformly distribute in the cell coverage which is rectangular region with size of $250(\text{m}) \times 300$ (m). The scenario features given in 3GPP TR 38.901 UMa were followed, using $N_f = 667$ subcarriers with $15K$-Hz spacing and $M_f = 55$ pilots with a downsampling ratio of $D_{\text{RS}} = 12$ as a common setting if not specified and assuming precise CSI estimates at the UEs. The NMSE metric was used to assess performance.

For DL-based models, we conducted training with a batch size of 32 for 1500 epochs, starting with a learning rate

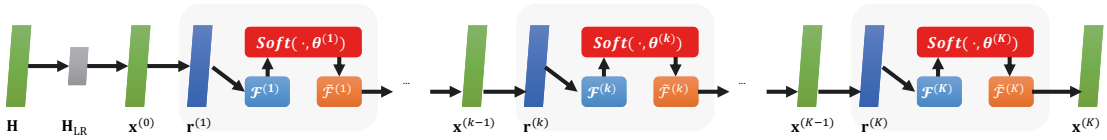

Fig. 10. Network architecture of ISTA-Net.

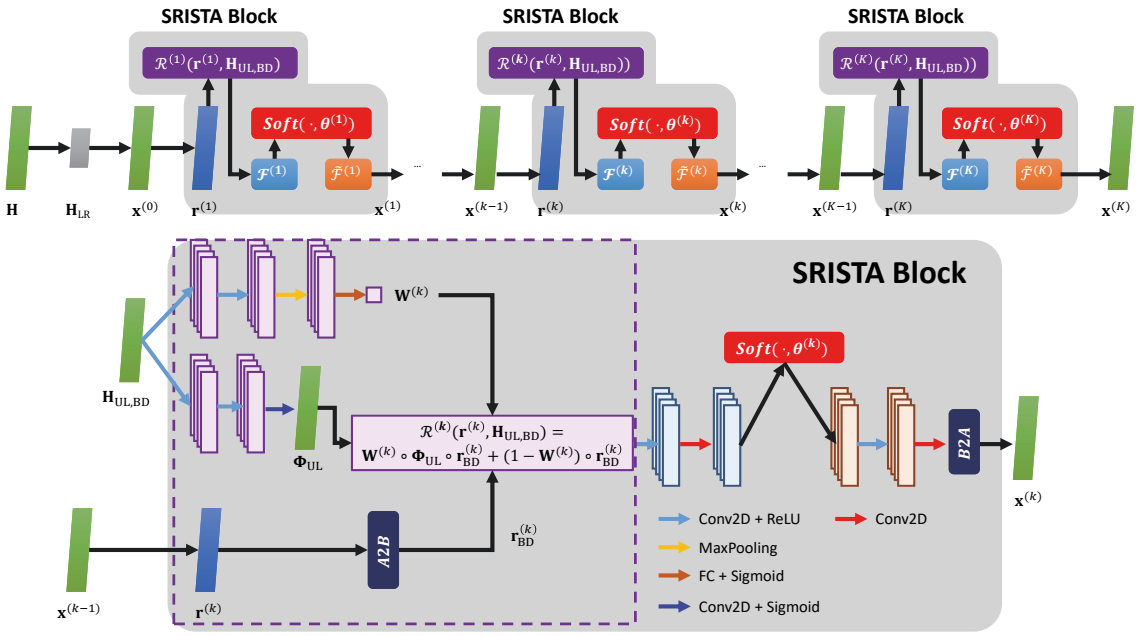

Fig. 11. Network architecture of SRISTA-Net. For the construction of $\mathbf{W}^{(k)}$, we employ a pair of 2D convolutional layers followed by max pooling operations. This approach is designed to refine the output, focusing it more acutely on specific segments of the side information. Subsequently, integrating a sigmoid layer as the terminal activation mechanism compels $\mathbf{W}^{(k)}$ to execute a binary fusion of the processed and unprocessed outcomes, specifically between $\mathbf{\Phi}_{\mathrm{UL}} \circ \mathbf{r}_{\mathrm{BD}}^{(k)}$ and $\mathbf{r}_{\mathrm{BD}}^{(k)}$. As for the generation of $\mathbf{\Phi}_{\mathrm{UL}}$, we apply BFD block in Eq. 4 mentioned in the previous section.

of 0.001 and setting an early stop criterion that validation loss does not improve for 100 epochs. We generated the outdoor datasets using QuaDRiGa channel simulators [42]. We consider 16 TTIs for each out of 2000 UEs. In total, the dataset consists of 32,000 channels. We used one-tenth of the channels for testing and validation, respectively. The remaining four-fifths channels are for training.

For the ease to evaluate the degree of aliasing, it is common to use delay spread as a performance metric. A channel with larger delay spread tends to suffer aliasing effects more severely since it contains more high-delay multipaths. We cluster all the 3200 test CSI data into 3 clusters according to their RMS delay spread: low (smaller than 500 ns), medium (inbetween 500 ns and 1000 ns), high-delay spread (larger than 1000 ns). The low, medium and high delay spread clusters have 883, 1221 and 1095 test cases and are denoted as CL1, CL2 and CL3, respectively.

B. UL Assisted Bandpass Filter Design for Anti-aliasing

Fig. 12 displays the NMSE performance of the UL masking method at various R levels compared to traditional interpolation across different CSI-RS placement densities. At a high CSI-RS density ($D_{\mathrm{RS}} = 3$), the performance disparity between these approaches is minimal, notable mainly in the complete test dataset and CL1. However, a typical D_{RS} value, being either 12 or 24, introduces a more significant aliasing effect. For $D_{\mathrm{RS}} = 12$, the performance divergence becomes more pronounced, as the NMSE metrics show effective mitigation of aliasing effects, particularly in the high-delay-spread cluster, CL3.

In Fig. 13, the NMSE performance of the UL masking approach at varying R levels for $D_{\mathrm{RS}} = 3, 6, 12$ is depicted. This figure reveals the sensitivity of the proposed method to the choice of the UL masking parameter R. In cases of CSI with intense aliasing effects, a higher R is necessary to effectively suppress the aliasing copies. Conversely, a large R might be excessively aggressive for channels with a low delay spread, potentially compromising the integrity of the actual delay peaks.

C. SRCsiNet

In addition to the two upsampling approaches mentioned in the previous subsection, we compare them with the proposed learning-based SRCsiNet and SR network, SRCNN [26] and

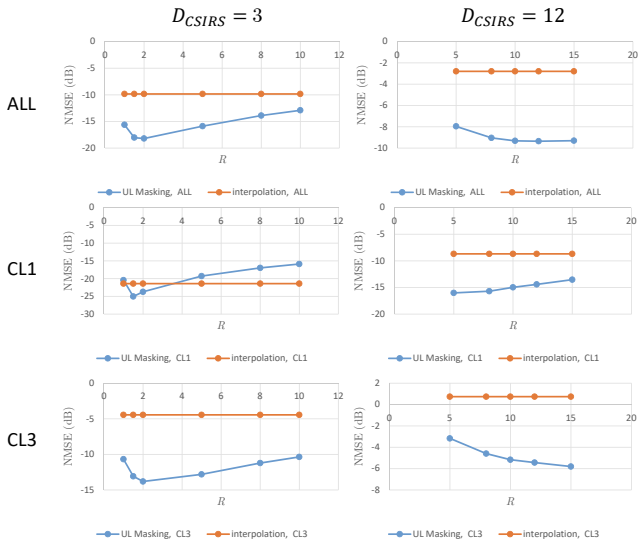

Fig. 12. NMSE performance of the proposed UL-assisted anti-aliasing and traditional linear interpolation for different CSI-RS placement densities ($D_{\text{RS}} = 3, 12$).

a deep unfolding framework, ISTA-Net [23]. Fig. 14 shows the NMSE performance of these alternatives for complete dataset and the three clusters. We can discover that ISTA-Net performs better than UL masking approach in CL1 due to the advantage of unfolding compressive sensing approach but performs poorly in CL3. That is because ISTA-Net does not introduce side information for dealing the aliasing effect. Clearly, by introducing UL CSI and providing flexibility in designing the bandpass filter, the overall performance can be improved by approximately 8 dB, which is significant. Fig. 15 shows the visualization of SRCsiNet. We can find that the bandpass filter design can effectively suppress the aliasing peaks and retain the delicate detail of the true peaks at the same time.

D. End-to-end CSI Recovery

In this subsection, we would like to demonstrate the importance of optimizing upsampling discrepancy for improving the overall performance. Table I shows the NMSE performance from the end-to-end, feedback, and upsampling operation for SRISTA-Net, Interpolation and ISTA-Net. End-to-end NMSE performance would be bounded by either feedback loss or upsampling discrepancy. Yet, we can first discover that the end-to-end performance is generally bounded by upsampling loss in the considered UMa channels. This means that upsampling loss plays an critical role for improving the overall performance. Lastly, we can also find that the end-to-end NMSE performance improvement is about 6-10 dB as compared to other upsampling approaches without introducing UL CSI information.

E. Solving Overfitting problem

The SRISTA-Net architecture, necessitating 0.2 million parameters, faces a significant challenge due to its size relative to the training data, often leading to overfitting issues. This subsection highlights the effectiveness of Data Augmentation (DA) in our approach. Table II presents the NMSE performance for varying numbers of virtual pilots, comparing scenarios before and after implementing DA. A major hurdle in deploying learning-based models at gNB is the acquisition of real CSI data. In our experiments, the training of the deep learning model utilized less than 30,000 data points. We observed that overfitting becomes a significant issue when relying solely on the original training dataset. To counter this issue, we implemented circular shifting, as suggested by [43], on the original training data in the angle domain, effectively doubling the training dataset size. This augmentation was found to markedly enhance NMSE performance, demonstrating the benefits of increased training data.

F. Temporal Sensitivity of SRISTA-Net

SRISTA-Net significantly surpasses other alternatives in NMSE performance. However, it is important to note that previous experiments were conducted under the assumption that both CSI-RS and virtual pilots are present within the same time slot[2]. Table III details the NMSE performance of SRISTA-Net, accounting for varying time gaps between CSI-RS and virtual pilots, alongside different counts of virtual pilots. Given the 10 ms periodicity of PBCH, PSS, and SSS, the maximum theoretical time difference between CSI-RS and virtual pilots is limited to under 5 ms. Our findings reveal that SRISTA-Net's performance is highly susceptible to even minimal time differences, such as 5 ms. Interestingly, the NMSE performance in scenarios with a 5-ms gap is observed to be inferior compared to cases without any virtual pilots. In conclusion, when CSI-RS and virtual pilots coexist in the same time slot, leveraging the additional information is beneficial. Otherwise, it is preferable to upscale the DL CSI without incorporating data from virtual pilots.

G. Complexity, Storage Requirements and Short Summary

Table IV outlines the complexity and storage requirements of all previously mentioned approaches. It is observed that while SRISTA-Net and ISTA-Net have similar model sizes and required similar complexities, SRISTA-Net significantly surpasses ISTA-Net in terms of performance. However, this comparison also highlights a drawback of deep unfolding methods. Due to the recursive application of convolutional operations on full-size data, these models exhibit higher complexity relative to others. Fortunately, the upsampling module in these models is implemented at the gNB. Considering the demands of future AI-enhanced cellular systems, a gNB equipped with multiple GPUs is envisioned, enabling real-time operation of such complex models. Nonetheless, there is an ongoing need to reduce the complexity of deep unfolding approaches, potentially through techniques like pruning [44], [45] or other methods of model size reduction.

Last but not least, to facilitate readers' understanding of our contributions, we provide Table V to highlight the key features

[2]It's assumed here that the CSI remains constant within the same time slot

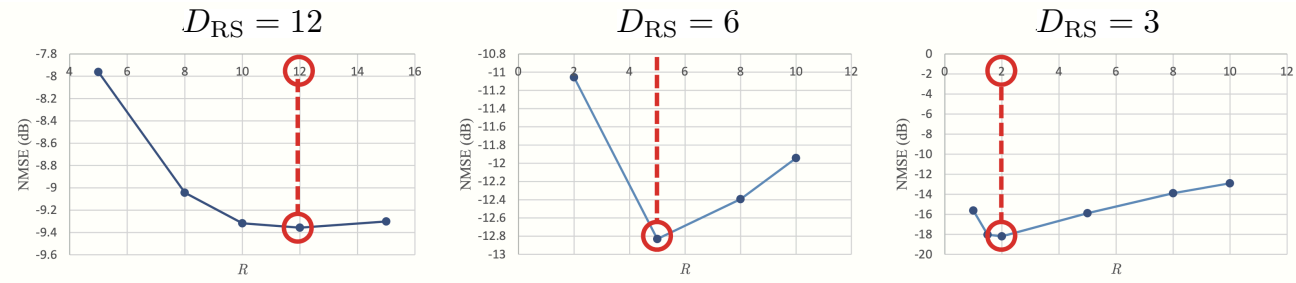

Fig. 13. NMSE performance of the proposed UL-assisted anti-aliasing for different CSI-RS placement densities ($D_{\mathrm{RS}} = 12, 6, 3$). We can clearly know that the optimal selection of the threshold level R varies with the aliasing effects. For the channels with strong aliasing effects, we require a larger R to suppress aliasing copies.

TABLE I
THE END-TO-END NMSE PERFORMANCE OF SRISTA-NET, INTERPOLATION AND ISTA-NET FOR DIFFERENT NUMBERS OF VIRTUAL PILOTS UNDER COMPRESSION RATIO IS 4.

P = 0					P = 64					P = 128				
DualNet-MP + SRISTA-Net					DualNet-MP + SRISTA-Net					DualNet-MP + SRISTA-Net				
	ALL	CL1	CL2	CL3		ALL	CL1	CL2	CL3		ALL	CL1	CL2	CL3
$Loss$	-12.8	-16.2	-12.5	-9.8	$Loss$	-15.5	-19.4	-15.8	-11.9	$Loss$	-17.5	-21.6	-17.9	-13.7
$Loss_{\mathrm{FB}}$	-14.5	-16.7	-13.6	-12.6	$Loss_{\mathrm{FB}}$	-19.6	-23.2	-19.7	-16.3	$Loss_{\mathrm{FB}}$	-22.2	-26.2	-22.7	-18.6
$Loss_{\uparrow}$	-17.2	-24.5	-18.0	-12.6	$Loss_{\uparrow}$	-17.6	-22.3	-18.7	-13.4	$Loss_{\uparrow}$	-19.4	-24.0	-20.1	-15.3
DualNet-MP + Interpolation					DualNet-MP + Interpolation					DualNet-MP + Interpolation				
	ALL	CL1	CL2	CL3		ALL	CL1	CL2	CL3		ALL	CL1	CL2	CL3
$Loss$	-2.7	-8.3	-1.9	0.7	$Loss$	-3.2	-8.9	-2.3	0.2	$Loss$	-3.6	-9.4	-2.8	-0.1
$Loss_{\mathrm{FB}}$	-14.5	-16.7	-13.6	-12.6	$Loss_{\mathrm{FB}}$	-19.6	-23.2	-19.7	-16.3	$Loss_{\mathrm{FB}}$	-22.2	-26.2	-22.7	-18.6
$Loss_{\uparrow}$	-2.7	-8.6	-1.9	0.7	$Loss_{\uparrow}$	-3.2	-9.0	-2.3	0.3	$Loss_{\uparrow}$	-3.6	-9.5	-2.8	-0.1
DualNet-MP + ISTA-Net					DualNet-MP + ISTA-Net					DualNet-MP + ISTA-Net				
	ALL	CL1	CL2	CL3		ALL	CL1	CL2	CL3		ALL	CL1	CL2	CL3
$Loss$	-6.7	-13.5	-8.1	-1.9	$Loss$	-13.3	-18.3	-14.2	-9.0	$Loss$	-14.3	-19.5	-15.4	-10.0
$Loss_{\mathrm{FB}}$	-14.5	-16.7	-13.6	-12.6	$Loss_{\mathrm{FB}}$	-19.6	-23.2	-19.7	-16.36	$Loss_{\mathrm{FB}}$	-22.2	-26.2	-22.7	-18.6
$Loss_{\uparrow}$	-7.2	-15.8	-9.1	-2.1	$Loss_{\uparrow}$	-14.5	-20.5	-15.9	-9.9	$Loss_{\uparrow}$	-15.3	-20.8	-16.5	-10.8

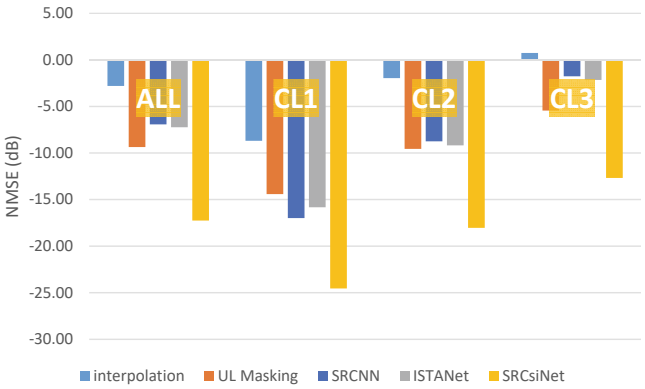

Fig. 14. NMSE performance of the learning based UL-assisted framework, SRCsiNet, and the alternatives in comparison for different clusters (i.e., all all samples and the samples with low, medium, large delay spread).

TABLE III
NMSE PERFORNACE OF SRISTA-NET FOR DIFFERENT TIME DIFFERENCES BETWEEN CSI-RS AND VIRTUAL PILOTS.

P = 64				
Time Difference	ALL	CL1	CL2	CL3
0ms	-17.6	-22.3	-18.7	-13.4
5ms	-13.6	-15.0	-14.1	-11.2
10ms	-9.2	-10.1	-9.5	-7.4
One-shot P=0	-17.2	-24.5	-18.0	-12.6
P = 128				
Time Difference	ALL	CL1	CL2	CL3
0ms	-19.40	-24.0	-20.1	-15.3
5ms	-11.7	-12.5	-11.9	-10.3
10ms	-6.2	-6.6	-6.3	-5.5
One-shot P=0	-17.2	-24.5	-18.0	-12.6

TABLE II
NMSE PERFORMANCE OF THE SRISTA-NET WITH AND WITHOUT DATA AUGMENTATION (DA).

P	Method	ALL	CL1	CL2	CL3
0	SRISTA-Net	-14.62	-21.34	-15.41	-10.12
	SRISTA-Net + DA	-16.88	-23.15	-17.73	-12.43
256	SRISTA-Net	-17.20	-22.48	-18.34	-12.83
	SRISTA-Net + DA	-20.55	-23.89	-20.81	-17.18

of the proposed approaches compared to previous rule-based and learning-based upsamplers.

VII. CONCLUSIONS

The proposed methods in this study present significant advancements in the recovery of downlink channel state information (CSI) in massive MIMO Frequency-Division Duplex-

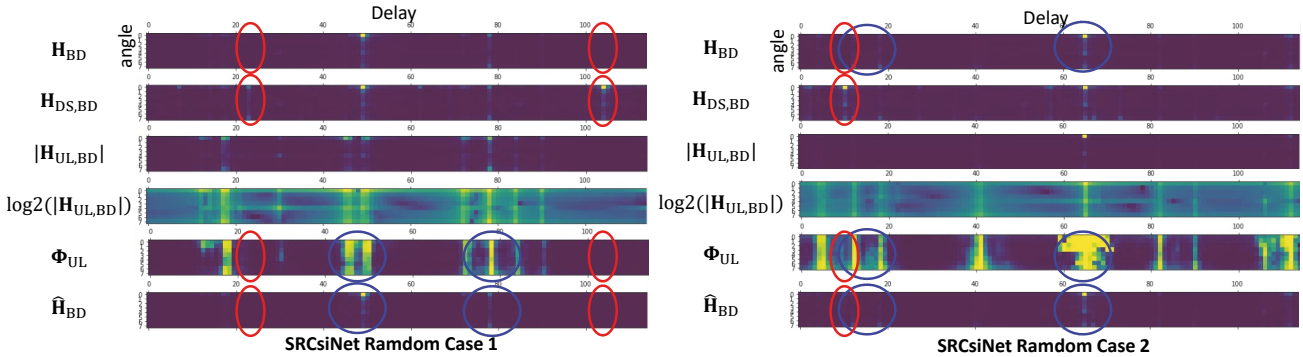

Fig. 15. Visual illustration of the results of the SRCsiNet. For the limited space, these examples only show the first 128 delay taps (we have 660 delay taps in the experiment). Since $D_{RS} = 12$, $\mathbf{H}_{\mathrm{DS,BD}}$ is periodic in every 55 delay taps. We can know from the examples that the bandpass filter works very well since it can capture very delicate details which are belong to true peaks (denoted by **blue** color circles) and suppress the aliasing peaks effectively (highlighted by **red** circles).

TABLE IV
STORAGE (PARA: MODEL PARAMETERS) AND COMPLEXITY (FLOPS) COMPARISON.

	PARA	FLOPs
Interpolation	0	109K
UL Masking	0	206K
SRCNN	63K	55.5M
ISTA-Net	196K	2G
SRCsiNet	7K	3.1M
SRISTA-Net	215K	2.01G

ing (FDD) systems, particularly addressing the issue of CSI undersampling caused by low-density pilot placement in modern cellular systems. The novel CSI upsampling framework, SRCsiNet, leverages the Discrete Fourier Transform (DFT) shifting theorem and multipath reciprocity, utilizing uplink (UL) CSI to effectively mitigate aliasing effects—a challenge that is particularly pronounced in high delay spread scenarios. The integration of this framework with the Iterative Shrinkage-Thresholding Algorithm Net (ISTA-Net), SRISTA-Net, further enhances the system's ability to handle non-uniform sampling, which is required for incorporating more side information for performance enhancement. The results demonstrate substantial benefits, with the proposed rule-based and deep learning methods outperforming traditional interpolation techniques and state-of-the-art approaches by 8-13 dB and 2-10 dB in terms of normalized mean square error, respectively. These findings highlight the robustness and effectiveness of the proposed methods, which not only provide superior CSI recovery but also maintain simplicity and efficiency, making them highly practical for deployment in modern communication systems. This work represents a significant step forward in addressing the challenges of CSI acquisition in massive MIMO FDD systems, setting a new benchmark for performance and reliability in wireless communications. For future researchers, it is important to address the issue of channel aging to build upon our work. In practical systems, the time lag between channel estimation and precoder execution at the UE and gNB sides, respectively, leads to outdated precoder relative to the current channel conditions. It is crucial to consider developing a joint framework that integrates both CSI upsampling and prediction to mitigate this issue effectively.

APPENDIX

To clarify the symbols to understand the problem formulation and equation better, we provide a summary of notations in Table VI.

REFERENCES

[1] L. Juho, H. Jin-Kyu, and J. Zhang, "MIMO technologies in 3GPP LTE and LTE-advanced," *EURASIP Journal on Wireless Communications and Networking*, vol. 2009, 12 2009.

[2] L. Zhao, K. Zheng, H. Long, and H. Zhao, "Performance analysis for downlink massive mimo system with zf precoding," *Transactions on Emerging Telecommunications Technologies*, vol. 25, no. 12, pp. 1219–1230, 2014.

[3] C. Wen, W. Shih, and S. Jin, "Deep Learning for Massive MIMO CSI Feedback," *IEEE Wirel. Commun. Lett.*, vol. 7, no. 5, pp. 748–751, 2018.

[4] T. Wang, C.-K. Wen, S. Jin, and G. Y. Li, "Deep learning-based csi feedback approach for time-varying massive mimo channels," *IEEE Wireless Communications Letters*, vol. 8, no. 2, pp. 416–419, 2019.

[5] Z. Lu, J. Wang, and J. Song, "Multi-resolution CSI Feedback with Deep Learning in Massive MIMO System," in *IEEE Intern. Conf. Communications (ICC)*, 2020, pp. 1–6.

[6] Q. Yang, M. B. Mashhadi, and D. Gündüz, "Deep Convolutional Compression For Massive MIMO CSI Feedback," in *IEEE Intern. Workshop Mach. Learning for Signal Process. (MLSP)*, 2019, pp. 1–6.

[7] S. Ji and M. Li, "CLNet: Complex Input Lightweight Neural Network Designed for Massive MIMO CSI Feedback," *IEEE Wirel. Commun. Lett.*, vol. 10, no. 10, pp. 2318–2322, 2021.

[8] Z. Liu, M. Rosario, and Z. Ding, "A Markovian Model-Driven Deep Learning Framework for Massive MIMO CSI Feedback," *IEEE Trans. Wirel. Commun.*, 2021, early access.

[9] J. Guo *et al.*, "DL-based CSI Feedback and Cooperative Recovery in Massive MIMO," *arXiv preprint arXiv:2003.03303*, 2020.

[10] Z. Liu, L. Zhang, and Z. Ding, "An Efficient Deep Learning Framework for Low Rate Massive MIMO CSI Reporting," *IEEE Trans. Commun.*, vol. 68, no. 8, pp. 4761–4772, 2020.

[11] ——, "Exploiting Bi-Directional Channel Reciprocity in Deep Learning for Low Rate Massive MIMO CSI Feedback," *IEEE Wirel. Commun. Lett.*, vol. 8, no. 3, pp. 889–892, 2019.

[12] Y.-C. Lin, Z. Liu, T.-S. Lee, and Z. Ding, "Deep Learning Phase Compression for MIMO CSI Feedback by Exploiting FDD Channel Reciprocity," *IEEE Wireless Commun. Lett.*, vol. 10, no. 10, pp. 2200–2204, 2021.

[13] Intel, "On NR Type I Codebook," TSG RAN WG1 No. 88 R1-1702205, 2021.

TABLE V

COMPARISON BETWEEN CSI UPSAMPLING APPROACHES IN TERMS OF DIFFERENT KEY FEATURES. HIGH-DS RECOVERY DENOTES THE ABILITY TO RECOVER HIGH-DS CSIS (4 IS THE BEST). NOTE THAT ISTANET MAY PERFORM BETTER THAN UL MASKING IF INTRODUCING VIRTUAL PILOTS.

	High-DS Recovery	FDD Reciprocity Utilization	Virtual Pilot Utilization	Model Size	Complexity	Support Non-uniform Upsampling
Interpolation	1	X	X	N/A	Low	X
UL Masking	2	O	X	N/A	Low	X
ISTANet	2*	X	O	High	High	O
SRCsiNet (Ours)	3	O	X	Low	Medium	X
SRISTANet (Ours)	4	O	O	High	High	O

[14] Samsung, "Type II CSI Reporting," TSG RAN WG1 No. 89 R1-1707962, 2021.

[15] L. Ramos *et al.*, "Mobile Channel Multipath Measurements andStatistical Characterization in Sub-6 GHz Bands," in *IMOC 2023*, 11 2023.

[16] K. Hanedaet *al.*, "5g 3gpp-like channel models for outdoor urban microcellular and macrocellular environments," in *2016 IEEE 83rd Vehicular Technology Conference (VTC Spring)*, 2016, pp. 1–7.

[17] "Study on channel model for frequencies from 0.5 to 100 GHz," *3GPP TR 38.901 version 14.3.0 Release 14*, 2018.

[18] T. T. S. Rappaport, S. Sun, R. Mayzus, H. Zhao, Y. Azar, K. Wang, G. N. Wong, J. K. Schulz, M. Samimi, and F. Gutierrez, "Millimeter wave mobile communications for 5g cellular: It will work!" *IEEE Access*, vol. 1, pp. 335–349, 2013.

[19] L. Zhao, K. Zheng, H. Long, and H. Zhao, "Performance analysis for downlink massive MIMO system with ZF precoding," *Transactions on Emerging Telecommunications Technologies*, vol. 25, no. 12, pp. 1219–1230, 2014.

[20] E. J. Candes and M. B. Wakin, "An Introduction To Compressive Sampling," *IEEE Signal Processing Magazine*, vol. 25, no. 2, pp. 21–30, 2008.

[21] Y. Zhao, H. Wang, Y. Zheng, Y. Zhuang, and N. Zhou, "High sampling rate or high resolution in a sub-Nyquist sampling system," *Measurement*, vol. 166, p. 108175, 2020.

[22] A. Beck and N. Teboulle, "A Fast Iterative Shrinkage-Thresholding Algorithm for Linear Inverse Problems," *Society for Industrial and Applied Mathematics*, vol. 2, no. 1, p. 183–202, Mar. 2009.

[23] J. Zhang and B. Ghanem, "ISTA-Net: Interpretable Optimization-Inspired Deep Network for Image Compressive Sensing," in *IEEE CVPR*, 06 2018, pp. 1828–1837.

[24] J. Guo, L. Wang, F. Li, and J. Xue, "CSI Feedback With Model-Driven Deep Learning of Massive MIMO Systems," *IEEE Wirel. Commun. Lett.*, vol. 26, no. 3, pp. 547 – 551, 2022.

[25] Z. Wang, J. Chen, and S. H., "Deep Learning for Image Super-Resolution: A Survey," *IEEE Trans. Pattern Anal. Mach. Intell.*, vol. 43, no. 10, pp. 3365–3387, 2021.

[26] C. Dong, C. Chen, K. He, and X. Tang, "Image Super-Resolution Using Deep Convolutional Networks," *IEEE Trans. Pattern Anal. Mach. Intell.*, vol. 38, no. 2, pp. 295–307, 2016.

[27] J. Fang, H. Lin, X. Chen, and K. Zeng, "A Hybrid Network of CNN and Transformer for Lightweight Image Super-Resolution," in *Proc. IEEE Comput. Soc. Conf. Comput. Vis. Pattern Recognit.*, June 2022, pp. 1103–1112.

[28] C.-H. Lin, W.-C. Kao, S.-Q. Zhan, and T.-S. Lee, "BsNet: A Deep Learning-Based Beam Selection Method for mmWave Communications," in *2019 IEEE 90th Vehicular Technology Conference (VTC2019-Fall)*, 2019, pp. 1–6.

[29] Q. Li, P. Sisk, A. Kannan, T. Yoo, T. Luo, G. Shah, B. Manjunath, C. Samarathungage, M. T. Boroujeni, H. Pezeshki, and H. Joshi, "Machine Learning Based Time Domain Millimeter-Wave Beam Prediction for 5G-Advanced and Beyond: Design, Analysis, and Over-The-Air Experiments," *IEEE Journal on Selected Areas in Communications*, vol. 41, no. 6, pp. 1787–1809, 2023.

[30] S.-C. Fan, H.-Y. Chang, C.-Y. Wang, and W.-H. Chung, "Super Resolution-Based Beam Selection With Hierarchical Codebook in mmWave Communication," *IEEE Wireless Communications Letters*, vol. 11, no. 5, pp. 967–971, 2022.

[31] Y.-C. Lin, T.-S. Lee, and Z. Ding, "A Scalable Deep Learning Framework for Dynamic CSI Feedback with Variable Antenna Port Numbers," *IEEE Trans. Wirel. Commun.*, pp. 1–1, 2023.

[32] R. Chataut and R. Akl, "Massive MIMO Systems for 5G and beyond Networks—Overview, Recent Trends, Challenges, and Future Research Direction," *Sensors*, vol. 20, no. 10, 2020.

[33] M. Soltani, V. Pourahmadi, A. Mirzaei, and H. Sheikhzadeh, "Deep Learning-Based Channel Estimation," *IEEE Commun. Lett.*, vol. 23, no. 4, pp. 652–655, 2019.

[34] E. Balevi, A. Doshi, and J. Andrews, "Massive MIMO Channel Estimation With an Untrained Deep Neural Network," *IEEE Trans. Wirel. Commun.*, vol. 19, no. 3, pp. 2079–2090, 2020.

[35] 3GPP, "NR; Physical Channels and Modulation," 3rd Generation Partnership Project (3GPP), Technical Specification (TS) 38.211, June 2020, version 16.6.0.

[36] L. Tan and J. Jiang, *Digital Signal Processing: Fundamentals and Applications*, 2nd ed. USA: Academic Press, Inc., 2013.

[37] Z. Zhong, L. Fan, and S. Ge, "FDD Massive MIMO Uplink and Downlink Channel Reciprocity Properties: Full or Partial Reciprocity?" in *GLOBECOM 2020 - 2020 IEEE Global Communications Conference*, 2020, pp. 1–5.

[38] F. Rottenberg, R. Wang, J. Zhang, and A. F. Molisch, "Channel Extrapolation in FDD Massive MIMO: Theoretical Analysis and Numerical Validation," in *2019 IEEE Global Communications Conference (GLOBECOM)*, 2019, pp. 1–7.

[39] H. Xu, J. Zhang, P. Tang, L. Tian, Q. Wang, and G. Liu, "An empirical study on channel reciprocity in tdd and fdd systems," *IEEE Open Journal of Vehicular Technology*, vol. 5, pp. 108–124, 2024.

[40] J. Guo, C.-K. Wen, and S. Jin, "CAnet: Uplink-Aided Downlink Channel Acquisition in FDD Massive MIMO Using Deep Learning," *IEEE Trans. Commun.*, vol. 70, no. 1, pp. 199–214, 2022.

[41] S. Gao, X. Liu, B. Zeng, S. Xu, Y. Li, X. Luo, J. Liu, X. Zhen, and B. Zhang, "Implicit Diffusion Models for Continuous Super-Resolution," in *Proc. IEEE Comput. Soc. Conf. Comput. Vis. Pattern Recognit.*, June 2023, pp. 10 021–10 030.

[42] S. Jaeckel *et al.*, "QuaDRiGa: A 3-D Multi-Cell Channel Model with Time Evolution for Enabling Virtual Field Trials," *IEEE Trans. Antennas and Propag.*, vol. 62, no. 6, pp. 3242–3256, 2014.

[43] Z. Liu, L. Wang, L. Xu, and Z. Ding, "Deep Learning for Efficient CSI Feedback in Massive MIMO: Adapting to New Environments and Small Datasets," *arXiv preprint arXiv:2211.14785*, 2023.

[44] G. T. Liang anb J, L. Wang, S. Shi, and X. Zhang, "Pruning and quantization for deep neural network acceleration: A survey," *Neurocomputing*, vol. 461, pp. 370–403, 2021.

[45] S. Han, H. Mao, and W. J. Dally, "Deep Compression: Compressing Deep Neural Network with Pruning, Trained Quantization and Huffman Coding," *Proc. IEEE Comput. Soc. Conf. Comput. Vis. Pattern Recognit.*, 2015.

TABLE VI
NOTATION SUMMARY

Notation	Description
General Notations	
N_a	Number of antennas at gNB
N_f	Number of subcarriers in each subband
Δf	Subcarrier spacing
D_{RS}	Pilot (CSI-RS) spacing in subcarriers
S_{F}	Pilot sample rate in frequency
M_f	Number of pilots (CSI-RS) in a BWP
N_f	Number of subcarriers in a BWP
$(\cdot)^H$	Conjugate transpose
$\|\cdot\|_F$	Frobenius norm
$\circ$	Element-wise product operation
$\mathbf{e}_i$	i-th column vector of an identity matrix of size N_f
$\mathbf{Q}_{D_{\text{RS}}}$	Downsampling matrix with pilot rate D_{RS}
Ψ_{RS}	Downsampling index set
Δt_{max}	Maximum delay tap
D	Number of random tests
$\mathbf{N}$	Channel estimation noise
$\mathbf{\Phi}$	Binary map for non-zero bin locations of $\mathbf{H}_{\text{BD}}$
Channel State Information (CSI) Matrices	
$\mathbf{h}_i$	RS CSI of the i-th antenna at gNB
$\mathbf{H}$	Full DL CSI matrix
$\mathbf{H}_{\text{RS}}$	RS CSI matrix
$\widehat{\mathbf{H}}_{\text{RS}}$	Estimated RS CSI
$\mathbf{H}_{\text{DS}}$	DS CSI matrix
$\mathbf{H}_{\text{BD}}$	Full DL CSI in BD domain
$\mathbf{H}_{\text{DS,BD}}$	DS CSI in BD domain
$\widehat{\mathbf{H}}$	Estimated DL CSI after upsampling
$\mathbf{H}_{\text{UL}}$	Full UL CSI matrix
$\mathbf{H}_{\text{UL,BD}}$	Full UL CSI matrix in BD domain
Transformations and Functions	
$\mathbf{F}_{\text{AB}}$	DFT matrix for antenna to beam domain
$\mathbf{F}_{\text{FD}}$	IDFT matrix for frequency to delay domain
$f_{\text{en}}(\cdot)$	Encoder function
$f_{\text{de}}(\cdot)$	Decoder function
$f_{\uparrow}(\cdot)$	Upsampling operation
$f_{\text{TPR}}(\cdot)$	True Peak Recovery function
$f_{\text{BFD}}(\cdot)$	Bandpass Filter Design function
$f_{\text{AR}}(\cdot)$	CSI Attention and Refinement function
Feedback and Loss Functions	
$\mathbf{q}$	Codeword for UL feedback
CR	Compression ratio
$Loss_{\text{FB}}$	Feedback loss
$Loss_{\uparrow}$	Upsampling loss
$\mathcal{L}_{\text{discrepancy}}$	Discrepancy loss
$\mathcal{L}_{\text{symmetry}}$	Symmetry loss
$\mathcal{L}_{\text{all}}$	Total loss
Compressive Sensing and ISTA-Net	
$\widetilde{\mathbf{F}}_{\text{FD}}$	Trimmed DFT transformation matrix
$\rho^{(k)}$	Trainable step size in ISTA-Net
$\mathcal{F}^{(k)}$	Function in ISTA-Net
$\widetilde{\mathcal{F}}^{(k)}$	Inverse function in ISTA-Net
$\mathbf{r}^{(k)}$	Intermediate result in ISTA-Net
$\mathbf{x}^{(k)}$	Result in ISTA-Net
$\mathcal{R}^{(k)}$	Reciprocity assisting function in SRISTA-Net
$\mathbf{W}^{(k)}$	Weight matrix in SRISTA-Net
$\mathbf{\Phi}_{\text{UL}}$	Bandpass filter generated using UL CSI
$\mathbf{H}_{\text{LR}}$	Low-resolution DL CSI
$\widetilde{\mathbf{H}}_{\text{LR}}$	Low-resolution CSI in AD domain
$\mathbf{I}$	Identity matrix
Φ_{P}	Pilot index set